IEEE Photonics Journal
An IEEE Photonics Society Publication

Open Access

Effect of Human Brain Edema on Light Propagation: A Monte Carlo Modeling Based on the Visible Chinese Human Dataset

Volume 9, Number 5, October 2017

Lanhui Wu
Yu Lin
Ting Li

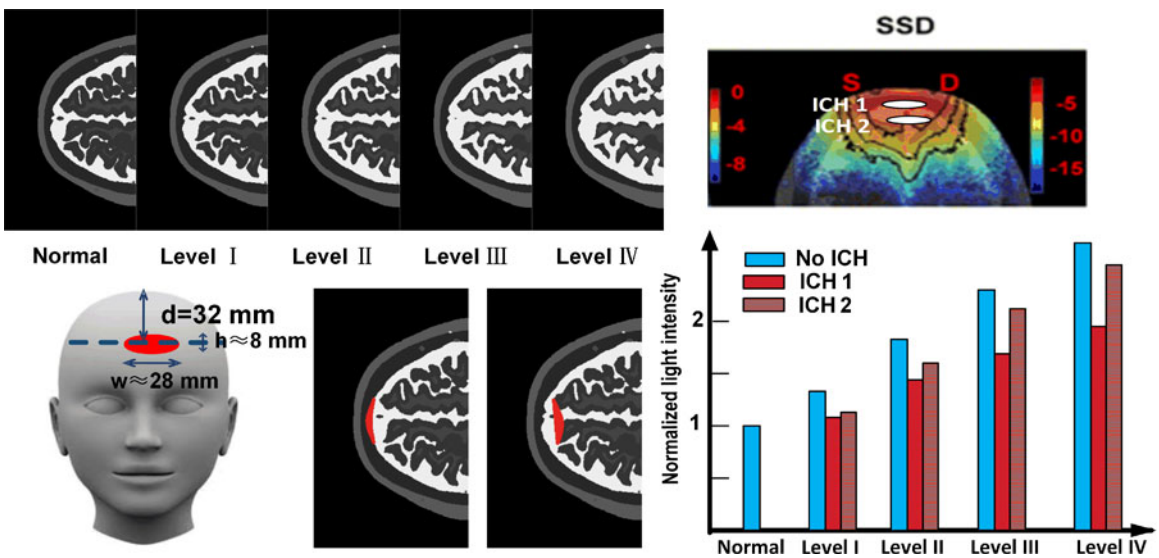

DOI: 10.1109/JPHOT.2017.2743048
1943-0655 © 2017 IEEE

Effect of Human Brain Edema on Light Propagation: A Monte Carlo Modeling Based on the Visible Chinese Human Dataset

Lanhui Wu,[1] Yu Lin,[2] and Ting Li[1]

[1]Institute of Biomedical Engineering, Chinese Academy of Medical Science and Peking Union Medical College, Beijing 300192, China
[2]North Carolina State University, Raleigh, NC 27606 USA

DOI:10.1109/JPHOT.2017.2743048

Manuscript received June 7, 2017; revised July 25, 2017; accepted August 16, 2017. Date of publication August 29, 2017; date of current version September 7, 2017. This work was supported in part by the One University One Zone Growth Fund under Grant A03013023001019, in part by the Fundamental Research Funds for the Central Universities under Grant ZYGX2016J052, in part by the CAMS Innovation Fund for Medical Sciences under Grant 2016-I2M-3-023, and in part by the National Natural Science Fund Projects under Grant 61675039. *(Lanhui Wu and Yu Lin contributed equally to this work.)*
Corresponding author: Ting Li (e-mail: liting@uestc.edu.cn).

Abstract: Brain edema originates from the excessive accumulation of cerebrospinal fluid (CSF) in the brain attributing to brain trauma or nontrauma diseases such as cancer, ischemic stroke, meningitis, and encephalitis. The high intracranial pressure could extrude the vessels in brain and block the blood circulation, yielding the risk of intracranial hemorrhage (ICH). In this study, we investigated the feasibility of utilizing functional near infrared spectroscopy (fNIRS) for brain edema inspection through Monte Carlo simulations over the head model of the Visible Chinese Human dataset. The outstanding influence of the development (4 levels) of edema and the occurrence of ICH on the light migration were observed. With the increase of CSF volume, the results show a strong linear relationship between the volumes of CSF and the intensities of the detected signal and the deeper penetration of photons. An outstanding contrast was also observed before and after the occurrence of ICH. The study revealed that fNIRS holds promise to be an easy and reliable solution for inspecting edema aggression inside brain through the observation on the variation of optical signals, and is very suitable for continuous bedside inspection.

Index Terms: Brain edema, functional near-infrared spectroscopy (fNIRS), light propagation, Monte Carlo simulation, visible Chinese human (VCH).

1. Introduction

Brain edema originates from the excessive accumulation of cerebrospinal fluid (CSF) in the brain attributing to brain trauma or non-trauma diseases such as cancer, ischemic stroke, meningitis, and encephalitis [1], [2]. Brain edema could lead to an abnormal increase in intracranial pressure (ICP) which can cause obstacles in brain function, irreversible pathological devastations in brain structures, and even brain death [3], [4]. In addition, a report also revealed that brain edema is a top-five disease of newborns in China. Nearly half of the infant patients may not survive within one and half a year. If not treated timely and effectively, the survivors can also continue suffering from laggard mental and physical development by contrast against normal children [5]. Intracranial hemorrhage

(ICH) is not only one of the reasons but also a complication of brain edema. The high intracranial pressure could extrude the vessels in brain and block the blood circulation, thus eventually yielding the blood to overflow through vascular walls into the CSF. One symbol of intracranial hemorrhage in hemodynamics is the increase of oxygen consumption and the resulting cerebral anoxia.

The development and recovery of brain edema can be directly reflected on the ICP change. The current measurement approach of ICP has to probe the cranial dura and/or ventricle by invasively inserting a sensor tip inside. This invasive operation will impose suffering and risk to patients [6]. The most reliable methodology for noninvasive brain edema detection and diagnosis are computed tomography (CT) imaging and magnetic resonance imaging (MRI) [7], [8]. The imagery of suspected brain area facilitates finding the brain edema and evaluating its range and degree of development. Yet, the utilization of these methods are always restrained by high cost, non-applicability to bedside and continuous monitoring, and exposure to radioactive beams (CT). Optical coherence tomography (OCT) also has been researched to monitor brain edema; however, the penetration depth of OCT is not sufficient for optical signals to significantly reach the brain [9]. It is a practical need to find a relatively simple and efficient solution to monitor brain edema, especially for the convenience of bedside inspection.

The detection of intracranial hemorrhage relies on the presence of blood in cerebrospinal fluid through ultrasound imagery and lumbar puncture. The invasive detection is suffering and may be late to the occurrence of ICH, though accurate. The online monitoring of ICH has been little researched yet.

Near-infrared spectroscopy (NIRS) offers a simple, fast, portable, relatively inexpensive method for noninvasive deep tissue hemodynamic monitoring [10]–[13]. Since invented in the 1970s, NIRS has been validated in many physiological conditions in brain research. In one type of NIRS technique using continuous-wave (CW) light, the photons at multiple wavelengths, typically ranging from 700 to 900 nm, penetrate through the biological tissues and the concentration change of hemoglobin is quantified through the variation in light intensity. The probing depth of fNIRS can be as large as centimeters, sufficient for penetrating the skull and reaching the human brain. Moreover, the differentiations in optical properties and oxygenation between blood and CSF make possible to be aware of the presence of blood in CSF instantly. The utilization of fNIRS for brain edema detection was preliminarily investigated in Ref. [14]. Though Monte Carlo (MC) simulation and phantom studies, the researchers showed that the intensity change of detecting light resulted mostly from the change of the thickness of cerebrospinal fluid (CSF) impacted rather than that of gray matter and white matter. However, this study simplified the brain as a layered structure without taking the actual complex structure of cerebral cortex folding geometry into account. The simulation based on this simplified model possesses barriers in reflecting the actual light propagation in the brain. The influence of ICH was not studied.

The present study adopted the head model of the Visible Chinese Human (VCH) dataset [15] to improve the accuracy of brain structure modeling and resultant light propagation variations. We performed the Monte Carlo simulations based on 3D vocalized media (MCVM) [16] to investigate the alternations, in different development levels of brain edema, in such as absorption, fluence, and spatial sensitivity distribution (SSD) in head comprehensively instead of light intensity alone. We also inspected the light variation caused by ICH. The results confirmed that the contrasts in optical signal can well reflect the changes in CSF volume and the presence of excessive blood in CSF.

2. Method

2.1 Monte Carlo Simulation

Monte Carlo simulation is extensively applied to model the light propagation in biological tissues. Various versions have been developed for diffuse research purpose and possess different features. The essential is somehow similar among these versions. In general, after a photon package (or a single photon depending on the specific version) enters a tissue media, it is about to be randomly scattered or absorbed by the particles in the media during its travel until “dies” or “escapes”. The

TABLE 1
Optical Properties of Tissue Component at 800 nm[20]

Tissue type	μ_a (cm^{-1})	μ_s (cm^{-1})	g	n
Scalp	0.10	187	0.81	1.37
Skull	0.16	160	0.90	1.43
Muscle	1.40	500	0.90	1.40
CSF	0.04	24	0.90	1.33
Gray matter	0.36	220	0.90	1.37
White matter	0.14	910	0.90	1.37
Blood	2.35	512	0.99	1.4

scattering and absorption events are mimicked by a series of function of possibility and survival criteria. The survived photons that can reach the detector will be collected and their status such as intensity and traveling path length will be analyzed for specific research purpose. In this study, we employed the version developed by our group previously, namely MCVM (Monte Carlo simulation based on 3D voxelized media). More specifically, a media, which can have arbitrary components and geometry, is modeled as an aggregate of cubic voxels with different properties (e.g., scattering coefficient, absorption coefficient, phase function, reflections, and refractions) and each voxel will be processed individually. The details of MCVM algorithm is described in Ref. [16].

2.2 VCH Head Model

The VCH dataset was developed on the basis of high-resolution whole body cryosectional color photograph sequence of a standing Chinese male adult (donated cadaver) with little pathological alternations. VCH has played an important role in many studies and its detail can be found in reference [15], [17]–[19].

In our study, the forehead part of VCH was divided into seven types of tissue, specifically including scalp, skull, muscle, CSF, gray matter, white matter, and blood vessels. The optical properties of each tissue component are given in Table 1 below where μ_a is the absorption coefficient, μ_s is the scattering coefficient, g is the anisotropic factor and n is the refraction index of the media. The values are from Ref. [14], [15], and [20]. For computer modeling, we appointed each voxel a cubic with $0.4 \times 0.4 \times 0.4\,mm^3$ in dimension and therefore eventually obtained $387 \times 231 \times 200$ voxels to present the structure of head. Please note that the voxels outside the brain were assigned as air and didn't participate in MC simulation. One slice of the brain of VCH with false colors is given in Fig. 1(a) as example.

2.3 Simulation Procedure and Data Processing

The anterior part of the VCH head model was used in this study. As shown in Fig. 1(b), a light source and a detector was placed respectively on the left and right side of forehead with a separation of 35 mm in between and a vertical distance of 32 mm to the top of the head. The total number of a photon package was 1×10^7 identically for each simulation. The detector was a circle with a radius of 1 cm mimicking a multimode fiber in practical utility.

An original cross-section of the VCH head model at the vertical level of source and detector (i.e., 32 mm to the top of the head) was illustrated in Fig. 1(c), namely "Normal". Since the major symptom of brain edema is the volume increase in CSF, a dilation and erosion function in software Photoshop

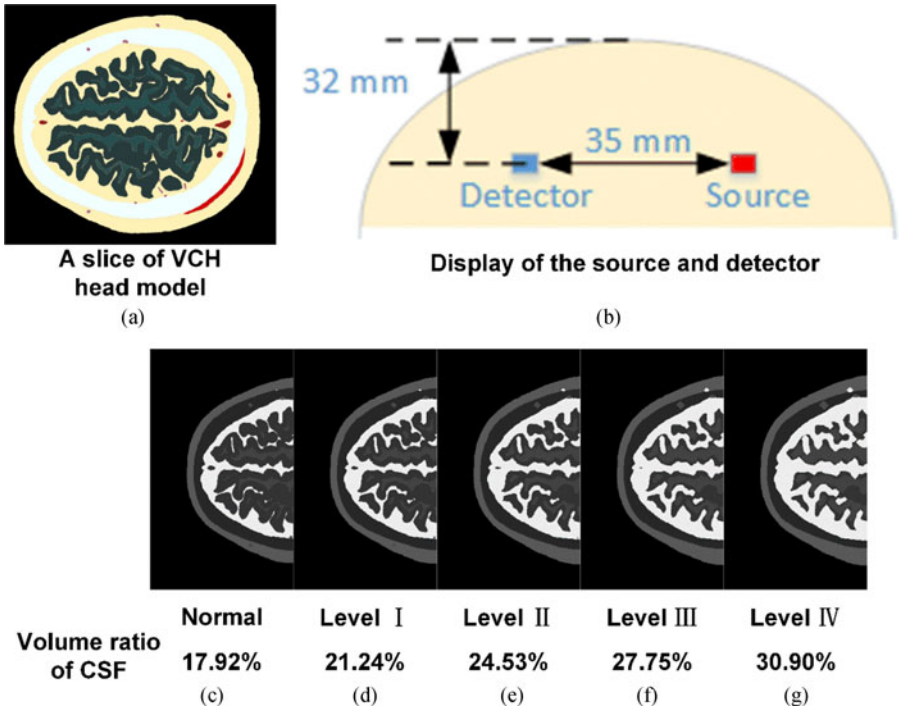

Fig. 1. The VCH head model and simulation settings, where (a) an original tissue-segmented image slice, (b) the placement of the light source and the detector, (c) the representative slice of normal head model at the level of source and detector pair; (d-f) the representative slice of the level I-IV head model.

was introduced to expand the area of CSF layer in direction to the cerebral tissue by layer upon the normal status (Fig. 1(c)) in order to simulate different level of pathologic alternation in CSF. In each level, as shown in Fig. 1(d) to (g), the approximated CSF volumes and the corresponding ratios to total head volume were respectively 1.00×10^5 mm^3 (Normal, 17.92%), 1.18×10^5 mm^3 (level I, 21.24%), 1.37×10^5 mm^3 (level II, 24.53%), 1.56×10^5 mm^3 (level III, 27.75%), and 1.74×10^5 mm^3 (level IV, 30.90%). The growth of CSF was isotropic towards the gray matters and roughly about 0.19×10^5 mm^3. The simulation was repeated for 10 times at each level and the average photon fluence was used to present light propagation outcomes. The light intensity of each level in the following presentation was normalized to the normal condition.

We also simulated the change of light propagation when intracerebral hemorrhage occurred by increasing the volume of "leaking" blood (100%) in CSF. Since ICH can occur anywhere in CSF, we randomly selected two errhysis locations, one clingy to the interior surface of the skull and the other close to the gray matter. As shown in Fig. 2, the two errhysis areas were crescent-shaped with a similar dimension of 8 mm in height (h), 4 mm in length (w) and 28 mm in central thickness. The volume was about 247 mm^3. The center of the errhysis areas were about 9 mm off the center of forehead. We compared the light intensity, in terms of the number of detected photons in an area with radius equal to 0.5 cm, contrast before and after the presences of the errhysis areas.

2.4 Data Analysis

The output file of MCVM program contains the photon absorption in every voxel of the whole tissue model. The spatial distribution of light absorption, a 3D matrix of $387 \times 231 \times 200$ voxels, can be obtained therefrom. We named this matrix $A(\vec{r}_s, \vec{r}_i)$ in equations, where $\vec{r}_i$ and $\vec{r}_s$ respectively denotes the positions of the ith voxel and the light source (Fig. 3). The absorption coefficient (tissue

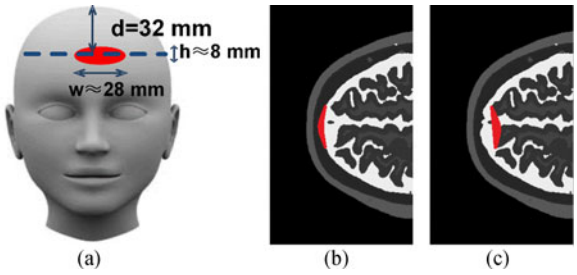

Fig. 2. The schematic diagram of intracerebral hemorrhage (ICH) in VCH head model, where (a) the locations and geometry of ICH in sagittal view, (b) ICH location 1 in sectional view, and (c) ICH location 2 in sectional review.

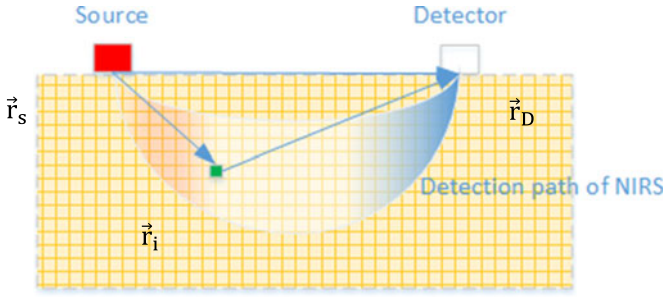

Fig. 3. The sketch map of detected NIRS signal path/sensitivity profile.

type specific) at the ith voxel is defined with $\mu_a(\vec{r}_i)$. 1 calculates the fluence, in terms of photon weight, across each voxel ($\vec{r}_i$) on light propagation from the light source location to this voxel.

$$\mathrm{F}(\vec{r}_s, \vec{r}_i) = \frac{A(\vec{r}_s, \vec{r}_i)}{\mu_a(\vec{r}_i)} \tag{1}$$

Then, we obtained signal sensitivity distribution (SSD) with three point Greens' function by (2). [21], which presents the influence of a voxel ($\vec{r}_i$) on total detected signal at the detector location $\vec{r}_D$ in two steps with $F(\vec{r}_s, \vec{r}_i)$ being from the light source ($\vec{r}_s$) to the ith voxel and $F(\vec{r}_D, \vec{r}_i)$ being from the ith voxel to the detector ($\vec{r}_D$),

$$\mathrm{SSD}(\vec{r}_s, \vec{r}_D, \vec{r}_i) = F(\vec{r}_s, \vec{r}_i) \times F(\vec{r}_D, \vec{r}_i) \tag{2}$$

The total SSD of each voxel was obtained by accumulating the SSD of each tissue type. In each voxel, the ratio of the SSD of a tissue type to total SSD represents the involvement of this tissue type in the light transportation in this voxel. The details can be found at Ref. [21].

3. Results

3.1 Light Intensity Increase

After having obtained the light intensity through MCVM simulation upon VCH head at each edema level (Fig. 1(d)–(g)), we normalized light intensities by dividing all those data by that of the normal status (Fig. 1(c)) referring to ref. [14]. Ref. [14] only showed the normalized light intensity increase following with CSF thickness, since the tissue model interrogated was a multilayered model. Here our data from VCH head model (Fig. 4) illustrates that the normalized light intensity increased in correspondence with the increase of CSF volume. A prominent linear relationship was observed through the linear regression analysis ($y = 13.866x - 1.534$, $r = 0.992$, $p < 10^{-5}$, where x is the volume ratio in decimal and y is the normalized light intensity), indicting the variation of light intensity

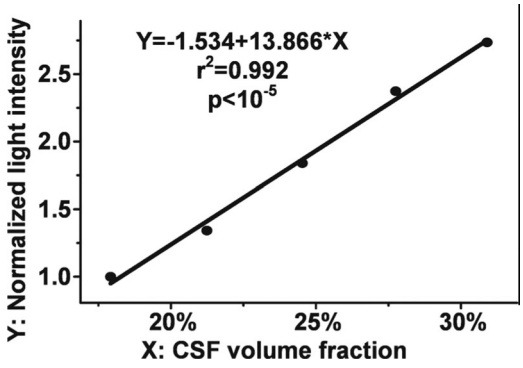

Fig. 4. The normalized light intensity variation with the CSF volume ratio in each brain edema level.

may be a practical and simple regime to reflect the deterioration or recovery level of edema in the manner of continuous bedside monitoring. Ref. [14] showed linear but slight increase at 4 cm S-D separation and not-well linear but significant increase at 3 cm separation, which partly support our findings (Fig. 4) which simulated at 3.5 cm separation. Referring to Table 1, the absorption coefficient and scattering coefficient of CSF, which primarily manipulate light attenuation in tissues, is much smaller than those of white matter and gray matter. When CSF excessively accumulates and shrinks the volume of other components (gray matter) in the detection path of fNIRS, the light intensity consequently increases.

3.2 Light Propagation

Fig. 5(a), and (b) separately displays the photon fluence and absorption distribution on the same slice of Fig. 1(c). The data were presented as the logarithm of the ration of photon fluence of the *i*th voxel (r_i) to that of incident light (r_s), i.e., $\log \frac{I(r_i)}{I(r_s)}$ and the logarithm of light absorption distribution, i.e., $A(\vec{r}_s, \vec{r}_i)$. Four contour lines were plotted in black in each subfigure, respectively for -1.5, -2.5, -3.5, and -4.5. As expected according to Fig. 3, the contours trend deeper in the course from Normal to Level IV, indicating that the photons can propagates deeper due to the low light attenuation of the increasing CSF.

3.3 Signal Sensitivity Distribution

Fig. 5(c) illustrates the spatial sensitivity distribution. Four contour lines represent the logarithm of SSD at -3, -4, -5 and -6 respectively in each subfigure. We didn't use the same contour level as Fig. 5(a) and (b) because the contour lines are too converging to be seen clearly. Since SSD reflects the involvement of one voxel to photon status changes (e.g., absorption,), deeper tissue got more involved in tissue interaction with photons, when photons travel further with the increase of CSF. It is also in excellent coincidence with Sections 3.1 and 3.2.

Table 2 introduces the proportion of SSD of each component under different edema levels. The proportion was the ratio of the total SSD of one components to the total SSD of all components and represented the contribution of each component to total signal. Muscle took very minor proportion in head components so that SSD of muscle responded little with the edema level change. Increases were observed in CSF and white matter due to the volume increase of CSF and deep photon propagation. However, the absolute SSD proportion of white matter was too small ($< 1\%$) to be a reliable criterion for brain edema assessment. The skull, blood, and scalp didn't participate in the growth of CSF and their SSD proportion decreased owing to the increase of total SSD caused by deeper propagation as well. The growth of CSF shrank the proportion of gray matter in the detection path of fNIRS, yielding the SSD decline of gray matter.

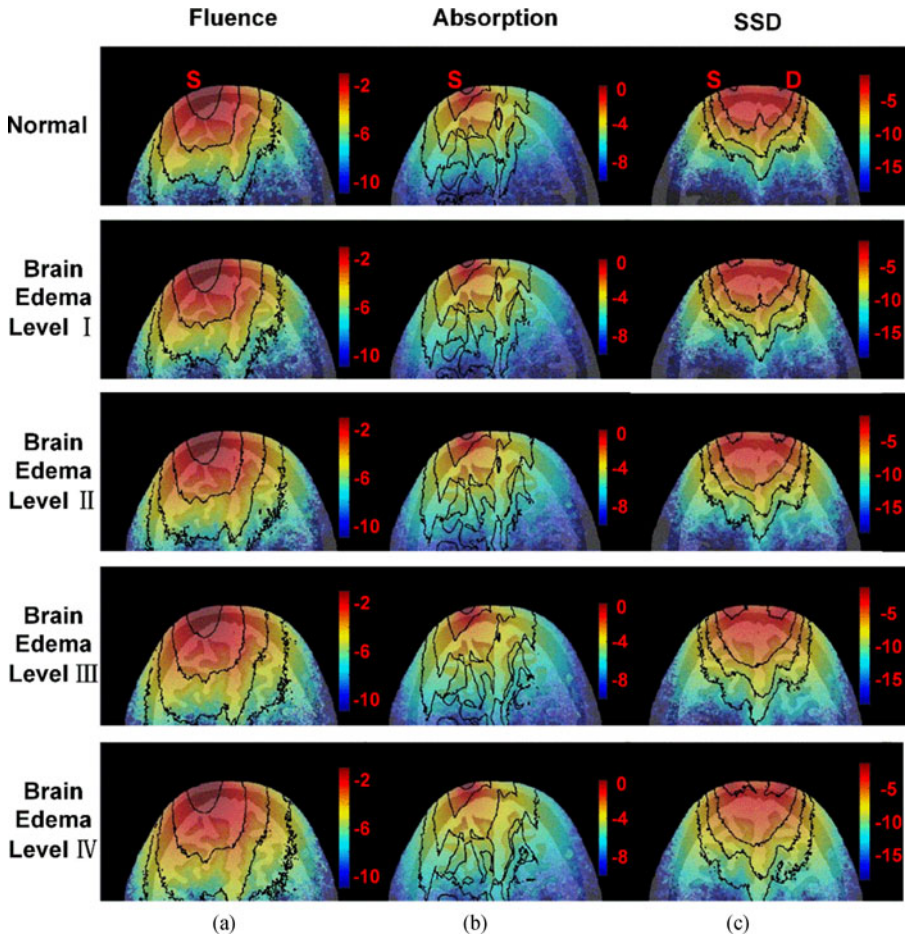

Fig. 5. The photon fluence (a), photon absorption (b), and the SSD (c) on the light source and detector located slice.

3.4 The Presence of ICH

Fig. 6(a) shows the change of light intensity normalized to the normal level before and after ICH occurred in two areas (ICH 1 for Fig. 2(b) and ICH 2 for Fig. 2(c)). We can clearly observe that the occurrence of ICH1 and ICH2 both yielded lower light intensity as photon explored more absorption and scattering events in blood than in CSF. From Level I to Level IV, for ICH 1 (the red bars), the light intensity drops were respectively 19.97%, 21.23%, 26.40% and 29.23% for ICH 1 (the red bars) and 16.6%, 12.73%, 7.69% and 7.68% for ICH 2 (the cyan bars). The contrast between red bars and cyan bars also strongly suggested that ICH 1 posed more influence than ICH 2 on light intensity variation. It is because, referring to Fig. 6(b), the region ICH 2 is located has relatively lower SSD is than where the ICH 1 is, making ICH 2 less involved in light propagation than ICH 1. The contrast of light variation were both outstanding anyway. Accordingly, a sudden change in light intensity in routine measurement could be used as a potential quantitative indicator of ICH.

4. Discussion and Conclusion

In this study, fNIRS showed encouraging potential in monitoring the progress of brain edema aggression. Though the presumptive diagnosis of brain edema has to currently reply on MRI or CT anyway due to the sensitivity of absolute fNIRS measurement to the diversity in optical properties and head structure between individuals, fNIRS offers a simple, less expensive, and reliable solution

TABLE 2
Proportion of SSD of Each Tissue Component in Different Level of Edema (Unit: %)

Stage	Scalp	Skull	Muscle	CSF	Gray matter	White Matter	Blood
Normal	34.07	35.53	0.01	24.08	5.56	0.01	0.63
Level I	33.57	34.19	0.01	26.24	5.45	0.06	0.47
Level II	33.22	32.94	0.01	28.19	5.22	0.14	0.28
Level III	33.16	31.69	0.01	29.97	4.81	0.27	0.01
Level IV	31.24	31.08	0.01	32.63	4.54	0.50	0.00

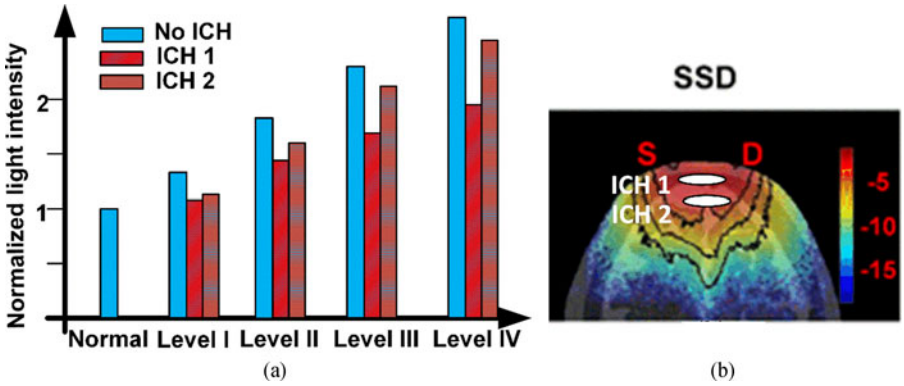

Fig. 6. The variation in light intensity induced by the presence of blood in CSF, where (a) is the normalized light intensity and (b) the approximated locations of blood presence in the SSD map.

for continuous bedside monitoring after the occurrence of edema is once confirmed in brain by other methodologies. The light intensity change was found approximately linear to the volume of CSF as demonstrated in Section 3.1. This provided an easy-to-observe reflection on edema aggression inside brain.

Compared with simplified brain structure in reference [14], the VCH head model provided more complex and more actual geometry of brain to investigate the light propagation in a more practical manner. Through this complex model, we revealed the involvement of each tissue type in light transportation and the change of light intensity after the occurrence of ICH. These findings can only be convincing and practical with this complex model since they are subject to the complexity of modeling.

Brain edema may not only occur in CSF but also in gray matter and white matter. In practical utilization, fNIRS signal may be required to reach deeper layers. The penetration depth of fNIRS is, as commonly believed, roughly half of the source-detector (S-D) separation. In this study, the source-detector separation was set at 35 mm allowing about 18 mm penetration. As shown in Fig. 4, this depth made the photon sufficiently explore the CSF and a part of gray matter. This encouraging finding indicates that fNIRS also holds prospect to inspect the combination of brain edema in CSF as well as gray matter.

According to Table 2, other than the alternation in SSD for each component, it is also should be noted that scalp and skull both took equivalent proportion in the total signal to the sum of CSF and gray matter. Skull usually will not produce any perturbance in measurement. However, scalp is possible, when outside enforces exist (contact pressure of probe and heating effect of laser), to

TABLE 3
Proportion of SSD of Each Tissue Component When the μ'_s of CSF was 90% of That in Normal Level

	Scalp	Skull	Muscle	CSF	Gray Matter	White Matter	Blood
Normal	33.49%	35.50%	0.01%	24.37%	5.96%	0.03%	0.64%
Level I	33.94%	34.03%	0.01%	25.88%	5.61%	0.07%	0.46%
Level II	32.34%	33.28%	0.01%	28.48%	5.45%	0.16%	0.28%
Level III	32.74%	31.69%	0.01%	30.13%	5.03%	0.30%	0.10%
Level IV	31.79%	31.04%	0.01%	32.03%	4.59%	0.53%	0.00%

induce significant interference to the measured light intensity and light propagation. To constrain this distortion, one can consider to use multiple S-D separation measurement to inspect both shallow layers and deep layers simultaneously.

The excessive accumulation of CSF will cram into the space of gray matter and white matter and therefore impose extra pressure to them. In the simulation, we employed a dilation and eroding function to extend the boundary of CSF to mimic the aggression of CSF at the cost of shrinking the volume of gray matter rather than "squeezing" it. This minor algorithm flaw may result in the decrease of the SSD of gray matter which is against that photons penetrate deeper in gray matter. In the future study, a more accurate expansion algorithm will be researched.

This study didn't discuss the impact of brain edema aggression on the optical properties of tissue such as scattering coefficients of gray matter and white matter. However, the impact may be relatively small compared with the volume change of CSF according to the reference [14], [20]. CSF occupies more portion than gray matter and white matter in signal sensitivity. This guess is supported by a preliminary simulation where we simply reduced the μ'_s of CSF to 90%. The SSD in Table 3 has minor difference from those in Table 2. There is no doubt that the larger change in optical properties will give rise to larger change in SSD and light intensity. Therefore, this trial needs to be investigated in the future. Moreover, blooding (aka, intracranial hemorrhage) sometimes accompanies the growth of CSF in the clinical manifestation of brain edema and increase the light absorption in CSF. Light intensity variation may not be reliable as a single parameter to reflect the development of brain edema. Multivariate investigation, such as frequency domain fNIRS or ultrasound, can be introduced to facilitate the reliability of fNIRS.

Intracranial hemorrhage was simulated in this study by replacing a part of tissue assignment of CSF with blood in two randomly selected areas. The results clearly shows that the outstanding difference in optical properties brought out saliency in light intensity change. Consequently, a sudden drop in light intensity may reflect the dramatic increase in blood. Future study would include more visible human dataset in simulation studies. We also applying for a clinical trial to take light intensity data on normal population to get the standard range for clinical diagnosis of brain edema with fNIRS. Since the region beneath the coverage of fNIRS probe contributes more sensitively to fNIRS measurement, the ICH that occurs away from this region may be detected as well, however, possibly with less reliability and sensitivity. This is a common issue of fNIRS technique. A solution to increase the coverage of probe may lie in enlarging the source-detector separation or widely arranging more light sources and detectors. Also, as mentioned above, the light intensity variation could be a comprehensive outcomes of various factors in the detected area, light intensity as a single contrast agent sometimes may possibly issue a false alarm of ICH. Multivariate modeling such as the incorporation of blood saturation, oxygen consumption and optical property may make the ICH prediction more reliable. Nevertheless, this study is the first, to the best of our knowledge, in investigating the inspection of ICH during edema with optical noninvasive approach.

To conclude, the present study employed the head model of Visible Chinese Human and Monte Carlo simulations to investigate noninvasively monitoring the development of brain edema and the occurrence of ICH intercurrent with brain edema. Light intensity was found to be straightforwardly correlated with the volume increase of cerebrospinal fluid. Photons can reach the cerebral tissue. The occurrence of ICH can outstandingly produce lower intensity, which can be used as a reflection on the presence of blood in CSF. Overall, this study demonstrated the great potential of fNIRS in monitoring brain edema.

References

[1] A. Raslan and A. Bhardwaj, "Medical management of cerebral edema," *Neurosurg. Focus*, vol. 22, 2007, Art. no. E12.
[2] J. A. Stokum, V. Gerzanich, and J. M. Simard, "Molecular pathophysiology of cerebral edema," *J. Cerebral Blood Flow Metabolism*, vol. 36, pp. 513–538, Mar. 2016.
[3] S. Nag, J. L. Manias, and D. J. Stewart, "Pathology and new players in the pathogenesis of brain edema," *Acta Neuropathologica*, vol. 118, pp. 197–217, Aug. 2009.
[4] D. Adukauskiene, A. Bivainyte, and E. Radaviciute, "Cerebral edema and its treatment," *Medicina-Lithuania*, vol. 43, pp. 170–176, 2007.
[5] G. Alper, I. T. Jarjour, J. D. Reyes, R. B. Towbin, W. L. Hirsch, and I. Bergman, "Outcome of children with cerebral edema caused by fulminant hepatic failure," *Pediatric Neurology*, vol. 18, pp. 299–304, Apr. 1998.
[6] R. M. Chesnut *et al.*, "A trial of intracranial-pressure monitoring in traumatic brain injury," *New England J. Med.*, vol. 367, pp. 2471–2481, Dec. 2012.
[7] C. Cristia *et al.*, "The association between a quantitative computed tomography (CT) measurement of cerebral edema and outcomes in post-cardiac arrest-A validation study," *Resuscitation*, vol. 85, pp. 1348–1353, Oct. 2014.
[8] D. Le Bihan, "Looking into the functional architecture of the brain with diffusion MRI," *Nature Rev. Neurosci.*, vol. 4, pp. 469–480, Jun. 2003.
[9] J. M. Schmitt, "Optical coherence tomography (OCT): A review," *IEEE J. Sel. Topics Quantum Electron.*, vol. 5, no. 4, pp. 1205–1215, Jul./Aug. 1999.
[10] D. Abookasis *et al.*, "Using NIR spatial illumination for detection and mapping chromophore changes during cerebral edema," *in Photonic Therapeutics and Diagnostics IV*. N. Kollias, B. Choi, H. Zeng, R. S. Malek, B. J. F. Wong, J. F. R. Ilgner, Eds. Bellingham, WA, USA: SPIE, 2008, vol. 6842, pp. 68422U.
[11] A. Villringer, J. Planck, C. Hock, L. Schleinkofer, and U. Dirnagl, "Near-infrared Spectroscopy (NIRS) – A new tool to study hemodynamic-changes during activation of brain-function in human adults," *Neurosci. Lett.*, vol. 154, pp. 101–104, May 1993.
[12] A. S. Gill, K. F. Rajneesh, C. M. Owen, J. Yeh, M. Hsu, and D. K. Binder, "Early optical detection of cerebral edema in vivo," *J. Neurosurg.*, vol. 114, pp. 470–477, Feb. 2011.
[13] A. Villringer and B. Chance, "Non-invasive optical spectroscopy and imaging of human brain function," *Trends Neurosci.*, vol. 20, pp. 435–442, Oct. 1997.
[14] Y. Liu, H. Wang, Y. Liu, W. Li, and Z. Qian, "Monte Carlo and phantom study in the brain edema models," *J. Innov. Opt. Health Sci.*, vol. 10, 2017, Art. no. 1650050.
[15] T. Li, H. Gong, and Q. M. Luo, "Visualization of light propagation in visible Chinese human head for functional near-infrared spectroscopy," *J. Biomed. Opt.*, vol. 16, Apr. 2011, Art. no. 045001.
[16] T. Li, H. Gong, and Q. M. Luo, "MCVM: Monte Carlo modeling of photon migration in voxelized media," *J. Innov. Opt. Health Sci.*, vol. 3, pp. 91–102, Apr. 2010.
[17] T. Li, Y. Li, Y. L. Sun, M. X. Duan, and L. Y. Peng, "Effect of head model on Monte Carlo modeling of spatial sensitivity distribution for functional near-infrared spectroscopy," *J. Innov. Opt. Health Sci.*, vol. 8, Sep. 2015, Art. no. 1550024.
[18] S. X. Zhang *et al.*, "The Chinese visible human (CVH) datasets incorporate technical and imaging advances on earlier digital humans," *J. Anatomy*, vol. 204, pp. 165–173, Mar. 2004.
[19] T. Li, C. Xue, P. Wang, and L. Wu, "Photon penetration depth in human brain for light stimulation and treatment: A Realistic Monte Carlo Simulation Study," *J. Innov. Opt. Health Sci.*, vol. 10, 2017, Art. no. 1743002.
[20] I. Nishidate, C. Mizushima, K. Yoshida, S. Kawauchi, S. Sato, and M. Sato, "In vivo estimation of light scattering and absorption properties of rat brain using a single-reflectance fiber probe during cortical spreading depression," *J. Biomed. Opt.*, vol. 20, Feb. 2015, Art. no. 27003.
[21] D. A. Boas, and A. M. Dale, "Simulation study of magnetic resonance imaging-guided cortically constrained diffuse optical tomography of human brain function," *Appl. Opt.*, vol. 44, pp. 1957–1968, Dec. 2005.